Heliyon 10 (2024) e26355

Contents lists available at ScienceDirect

Heliyon

journal homepage: www.cell.com/heliyon

Research article

Blood flow effects in a patient with a thoracic aortic endovascular prosthesis

Juan P. Tello [a,*], Juan C. Velez [a], Alberto Cadena [b], Andres Jutinico [c], Mauricio Pardo [a], Winston Percybrooks [a]

[a] Universidad del Norte, Km. 5 Via Puerto Colombia, Barranquilla, Colombia
[b] Clinica de la Costa, Barranquilla, Colombia
[c] Universidad Distrital Francisco Jose de Caldas, Bogota, Colombia

ARTICLE INFO

Dataset link: https://uninorte-my.sharepoint.com/:f:/g/personal/telloj_uninorte_edu_co/EmuXWKeFsnNAuWY5CYfCwu4BRGOcbQi_MadMJxg7Czauqw?e=z4oVxr

Keywords:
Blood flow
Velocity profiles
Pressure distributions
Image processing
Aorta
Cross section
Endovascular prosthesis

ABSTRACT

This work analyzes hemodynamic phenomena within the aorta of two elderly patients and their impact on blood flow behavior, particularly affected by an endovascular prosthesis in one of them (Patient II). Computational Fluid Dynamics (CFD) was utilized for this study, involving measurements of velocity, pressure, and wall shear stress (WSS) at various time points during the third cardiac cycle, at specific positions within two cross sections of the thoracic aorta. The first cross-section (Cross-Section 1, CS1) is located before the initial fluid bifurcation, just before the right subclavian artery. The second cross-section (Cross-Section 2, CS2) is situated immediately after the left subclavian artery. The results reveal that, under regular aortic geometries, velocity and pressure magnitudes follow the principles of fluid dynamics, displaying variations. However, in Patient II, an endoprosthesis near the CS2 and the proximal border of the endoprosthesis significantly disrupts fluid behavior owing to the pulsatile flow. The cross-sectional areas of Patient I are smaller than those of Patient II, leading to higher flow magnitudes. Although in CS1 of Patient I, there is considerable variability in velocity magnitudes, they exhibit a more uniform and predictable transition. In contrast, CS2 of Patient II, where magnitude variation is also high, displays irregular fluid behavior due to the endoprosthesis presence. This cross-section coincides with the border of the fluid bifurcation. Additionally, the irregular geometry caused by endovascular aneurysm repair contributes to flow disruption as the endoprosthesis adjusts to the endothelium, reshaping itself to conform with the vessel wall. In this context, significant alterations in velocity values, pressure differentials fluctuating by up to 10%, and low wall shear stress indicate the pronounced influence of the endovascular prosthesis on blood flow behavior. These flow disturbances, when compounded by the heart rate, can potentially lead to changes in vascular anatomy and displacement, resulting in a disruption of the prosthesis-endothelium continuity and thereby causing clinical complications in the patient.

* Corresponding author.
E-mail addresses: telloj@uninorte.edu.co (J.P. Tello), jcvelez@uninorte.edu.co (J.C. Velez), acadenabon@gmail.com (A. Cadena), aljutinicoa@udistrital.edu.co (A. Jutinico), mpardo@uninorte.edu.co (M. Pardo), wpercyb@uninorte.edu.co (W. Percybrooks).

https://doi.org/10.1016/j.heliyon.2024.e26355
Received 13 June 2023; Received in revised form 8 February 2024; Accepted 12 February 2024

Available online 20 February 2024

1. Introduction

For the present work, the following objectives can be established. Firstly, the impact of blood flow at the proximal edge of the endoprosthesis is aimed to be understood by examining hemodynamic patterns that can lead to the anticipation of possible prosthesis-endothelium detachment. Additionally, the hemodynamic responses (velocity profiles, pressure distributions, and wall shear stress - WSS) of two specific patients (PI and PII), one of them with an endovascular prosthesis, are compared in two cross sections of the aorta (CS1 and CS2). CS2 - PII is located at the endovascular prosthesis border to identify potential issues in the proximity of the prosthesis location. Based on the differences in the selected parameters, a preliminary step is taken in this study toward conducting a broader investigation to make significant generalizations for the benefit of patients who have required or will require prosthesis-based treatments for their cardiovascular conditions.

It is important to note that cardiovascular diseases (CVD) are one of the leading causes of the highest number of deaths in the world [1]. CVD accounted for approximately 19.05 million deaths worldwide in 2020 [2].

The Pan American Health Organization (PAHO) emphasizes the importance of prevention and treatment of CVD, with hypertension being the most common cardiovascular disease in Latin America and the Caribbean. In addition to the Non-communicable Diseases Risk Factor Collaboration (NCD-RisC) shows that people are unaware of their hypertension status, being higher in men (43%) than in women (28%) [3], [4].

For those with cardiovascular disease, the COVID-19 represents cause for alarm, and those with heart disease and stroke have an increased risk of developing severe forms of disease such as myocardial infarction, myocarditis, heart failure, shock, arrhythmias, and sudden death and stroke. [5].

One of the main underlying pathological processes that leads to heart attacks (coronary heart disease) and strokes (cerebrovascular disease) is known as atherosclerosis. Atherosclerosis is an inflammatory process affecting medium and large-sized blood vessels throughout the cardiovascular system [6]. In atherosclerosis, fatty material and cholesterol are deposited inside the lumen of medium and large-sized blood vessels (arteries). These deposits (plaques) cause the inner surface of the blood vessels to become irregular and the lumen to become narrow, making it harder for blood to flow [7].

A well-established relationship exists between certain cardiovascular diseases and blood flow [8]. Early atherosclerotic lesions have been observed to develop in regions where vessel branching occurs, resulting in complex or multidirectional flow patterns [9]. Therefore, obtaining a comprehensive description of blood flow characteristics holds clinical value. Presently, non-invasive techniques are employed to measure and characterize actual blood flow in specific patients. However, in many cases, these solutions lack the precision and spatio-temporal coverage required to be truly useful [10]. In such scenarios, simulations based on mathematical models emerge as a promising alternative.

Cardiovascular mechanics is a computational tool that has made it possible to create 2D simulation models, and it has evolved to more complex 3D models. These simulations aim to enhance our understanding and prediction of cardiovascular problems, all of which must be supported by mathematical models [9].

Similarly, with the assistance of Computational Fluid Dynamics (CFD), various studies have documented the simulation of blood flow in specific aortic models for individual patients [11], [12], [13].

The initial imaging-based Computational Fluid Dynamics (CFD) analyses were driven by the objective of investigating the impact of hemodynamic forces on the development of atherosclerosis in the carotid and coronary arteries. Additionally, they aimed to quantify hemodynamic forces on abdominal aortic aneurysms and develop personalized surgical protocols [14].

Using the Navier-Stokes mathematical model and various software tools for medical image processing and editing [15], along with computational methods, including Computational Fluid Dynamics (CFD), scientists have been exploring the behavior of blood flow and its interaction with vessel walls. Their goal is not only to quantitatively describe hemodynamic parameters but also to potentially identify or predict various vascular pathologies or complications [11], [16], [17], [18], [30], [19], [20], [21].

There is evidence of alterations in pressure values at the edge of the prosthesis (bird-beak), which may, at some point, impact the risk of prosthesis detachment [22], [23]. Hence, the main condition that triggers this study comes from developing new complications after Thoracic Endovascular Aortic Repair (TEVAR). Such complications present an opportunity to explore the mechanical and cellular mechanisms to explain this phenomenon. Abnormal flows leading to abnormal forces and subsequent deformation of the aorta have been observed at various levels within the circulatory system, such as aortic dilation in bicuspid valves and post-stenosis dilations. Potential complications of TEVAR at the proximal landing site may include the development of a new entry tear, either due to the formation of a new aneurysm or loss of seal. The abnormal wall shear stress (WSS) created at the landing site can, over time, account for why certain prostheses fail. Currently, the assessment of complications is reliant on frequent imaging. By employing non-invasive imaging techniques to evaluate mechanical forces, we can distinguish patients who may require more intensive imaging due to increased WSS-induced deformation of the aortic wall and, accordingly, plan personalized treatments. The development of new complications after TEVAR creates a possibility for the evaluation of mechanical and cellular mechanisms that explain the phenomenon. The evaluation of abnormal flows creating abnormal forces with subsequent deformation of the aorta has been observed at different levels in the circulatory system (aortic dilation in bicuspid valves, post-stenosis dilations). The potential complications of TEVAR in the proximal landing site include a new entry tear (either by new aneurysm formation or seal loss). The abnormal WSS created at the landing site can explain, over time, why some prostheses fail. Today, complications are diagnosed through frequent imaging. The evaluation of mechanical forces by non-invasive images can help differentiate patients who might require more intensive imaging due to increased WSS deformation of the aortic wall and plan personalized treatments.

This paper presents a study on the behavior of blood flow velocity profiles and pressure distributions in a 3D model of the aorta for two specific patients, investigating the influence of endovascular prostheses on flow patterns, particularly at the proximal edge.

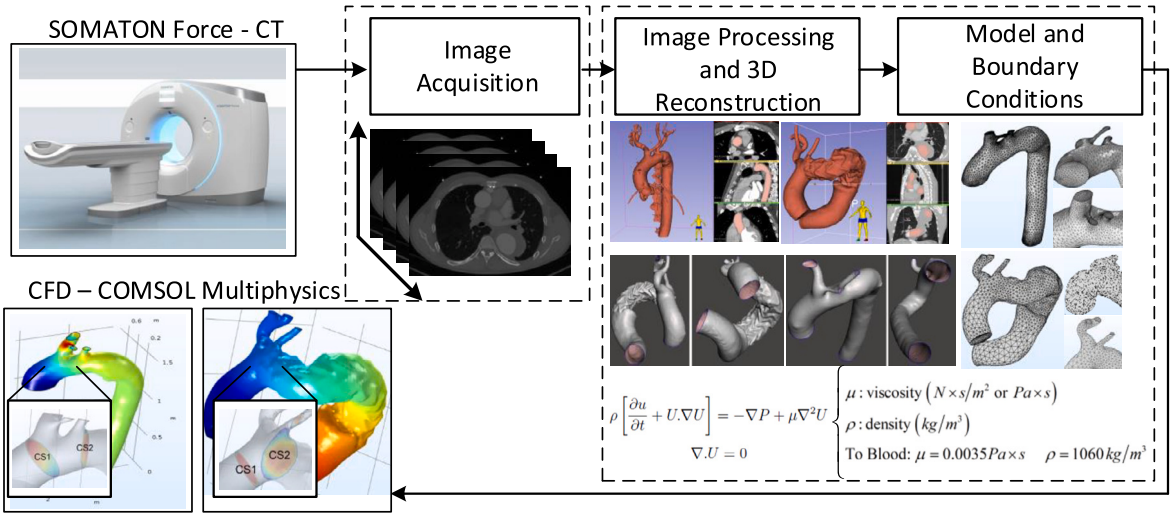

Fig. 1. Block diagram of the methodological process.

The study commences with the acquisition of Computerized Tomography (CT) scan images, followed by pre- and post-processing of the images to create 3D models of the aortas. Subsequently, blood flow is simulated using Comsol Multiphysics 5.3a software. Simulation results are recorded and analyzed at two cross-sections, at different predefined positions, and under specific initial conditions representative of a cardiac cycle.

This study aims to provide information on blood flow patterns (velocity, pressure and WSS) at specific positions and at important moments of the cardiac cycle at the edge of the prosthesis, providing additional insights into the problem of potential risk of prosthesis displacement.

The main contributions of the paper can be summarized as:

- The continuous collision of blood with the proximal edge of the prosthesis leads to significant variations in velocity profiles and pressure differentials, often exceeding 10% of their nominal values. This increase results in variations in shear forces, which, over time, can transmit deformations to the ends of the endoprosthesis, hindering its proper anchorage. This observation strengthens our hypothesis regarding the adverse effects on blood flow behavior upon contact with the proximal edge of the endoprosthesis.
- The observation that alterations in velocity profiles and pressure distributions at the prosthesis edges are propagated throughout the entire cross-sectional area of the aorta, generating vortices that disrupt blood flow stability and extend throughout its structure, raises concerns about potential displacements of the prosthesis anchor.
- The implementation of an adjustment mechanism in image acquisition synchronized with the heartbeat (triggered) is effective in minimizing artifacts in the ascending aorta. This is crucial due to the image acquisition time and the individual intrinsic movement of the heart, which varies for each patient. The synchronization mechanism is achieved by reducing the acquisition time (increasing the gantry velocity), lowering the heart rate, or using a combination of both strategies. Consequently, the obtained images can be accurately utilized for 3D modeling reconstruction. Subsequently, the 3D model serves as a valuable resource for redundancy and for reliable simulations of blood flow behavior within the aorta.

2. Materials and methods

The methodological process used for obtaining graphical and numerical values of velocity, pressure, and WSS in the aorta follows the scheme shown in Fig. 1. It starts from image acquisition and continues through simulation to the subsequent graphical representation of the results.

2.1. Image acquisition

In tomography images of the heart, the concept of temporal resolution, which refers to the timing of image acquisition, holds particular significance. Since the object under evaluation exhibits motion during image capture, it gives rise to artifacts. Therefore, it becomes imperative to implement a synchronization mechanism that enables the study of the beating heart. This synchronization is achieved by reducing the acquisition time (by increasing the gantry velocity), lowering the heart rate, or employing a combination of both processes. The artifacts stemming from the inherent cardiac movement extend into the ascending aorta, causing changes in its diameter from systole to diastole. Hence, it is necessary to adjust the acquisition to the heartbeat (triggered) to obtain images amenable to evaluation.

Using the exposed acquisition mechanisms, two patients are selected for the study of thoracic aortic vascular hemodynamics using CFD. The first patient, 72 years old, with aortic stenosis and other associate diseases (Patient I). The second, 68 years old, with

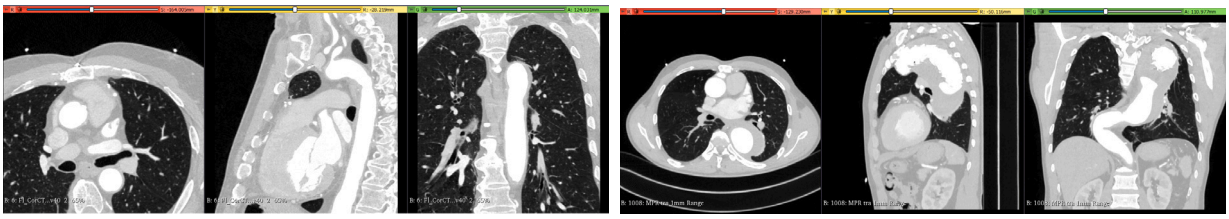

(a) Planes - Patient I (b) Planes - Patient II

Fig. 2. Axial, sagittal and coronal planes of Patients I and II.

proximal descending aortic aneurysm treated with aortic endoprosthesis (Patient II). Three-dimensional geometry is reconstructed from the CT scan (Sommaton Force CTAWP757474 by Siemens, owned by Clinica De La Costa in Barranquilla, Colombia) images with a resolution of 512×512, with a pixel size of 0.625 *mm* and with thickness of 0.6 *mm*. The medical DICOM images where anonymized to protect patients privacy. Figs. 2(a) and (b) shows an image for three different planes: axial, sagittal and coronal, for both patients.

2.2. Image processing and 3D reconstruction

The geometric characteristics of the three-dimensional model of a blood vessel for a specific patient are a necessary and decisive condition for obtaining flow patterns and shear stresses [24], [25], [26], [27], [28]. Similarly, vascularity varies among individual patients. Due to anatomical complexity and the presence of adjacent interfering tissues, such as bones or other tissues with similar intensities, the extraction of blood vessels is a laborious and time-consuming process. This can easily lead to error-prone diagnostic results in clinical practice [29]. Therefore, the acquisition and processing of images play a crucial role in adapting and obtaining a geometric structure that anatomically aligns with the region of interest.

Many previous studies have constructed simplified or idealized 3D geometries of the thoracic aorta using a limited series of two-dimensional slices initially obtained through conventional CT or magnetic resonance imaging (MRI). Techniques such as cubic spline curves have been employed to create models of the aortic cross-sections, often replacing the missing or idealized cross-sections of the subjects. With advancements in CT technology, there has been a significant improvement in the acquisition of multiple high-quality images, enabling the reconstruction of 3D models that closely resemble the real geometry of the aorta. However, the presence of artifacts caused by the intrinsic movement of the region of interest during acquisition still poses a challenge.

Bracamonte et al. [30] replace irregular cuts with circles of the same area and centroid to construct a solid object with smooth and regular surfaces. Morris et al. [25] generated three different three-dimensional models. The first model is based directly on CT scanner images without synchronization with the heart. The second model utilizes a method developed by Moore et al. in their previous works [31], [32], where the area of each axial slice is smoothed, leading to a modification of the (x, y) coordinates of the centroid. The third model assumes that all cross sections are concentric circles, which are also smoothed, with radii and areas determined for each acquired image.

In this study, the synchronization mechanism in the acquisition process, as described in the previous section, is utilized to prepare the acquired images for the subsequent stages. Three-dimensional aortic geometries for two patients are reconstructed from the CT images previously obtained. All images (382 for Patient I and 341 for Patient II) are processed to enhance the quality of the CT scans and generate 3D aortic geometries.

The open-source medical image processing software, *3dSlicer*, is employed for this purpose. The image processing workflow begins with contrast adjustment and noise reduction filters, followed by image segmentation to isolate the region of interest (ROI) using a thresholding algorithm. The software enables the 3D model of the aorta to be obtained. Notably, the resulting 3D model can be visualized during the image processing, facilitating subjective evaluation and the fine-tuning of image processing algorithms for greater accuracy.

The reconstructed model may include other structures, such as bones and parts of the heart muscle, which need to be manually removed to visualize the ROI correctly. Tools are provided by the software for the removal of undesired structures and the visualization of the model's edges. Cross-sections perpendicular to the blood vessel axis are created using MeshMixer software (https://www.meshmixer.com/) to further refine the model and differentiate the aorta from other vessels. These cross-sections are also used to smooth out irregularities and highlight the features of the aorta.

Figs. 3(a) and (b) display the 3D geometries after processing, and these geometries are loaded onto Academic Classkit License - Comsol Multiphysics 5.3a software. In Comsol Multiphysics, the meshing process is performed, as shown in Figs. 3(c) and (d).

3. Model and boundary conditions

A CFD model is proposed for the hemodynamic analysis of aortic geometries, as illustrated in Fig. 3. The mathematical model for blood flow velocity and pressure is computed using the Navier-Stokes equations [17], [11], [33]. Assuming an incompressible, unstable laminar flow and neglecting the influence of gravity, it can be stated that

$$\rho\left[\frac{\partial u}{\partial t} + U.\nabla U\right] = -\nabla P + \mu\nabla^2 U \tag{1}$$

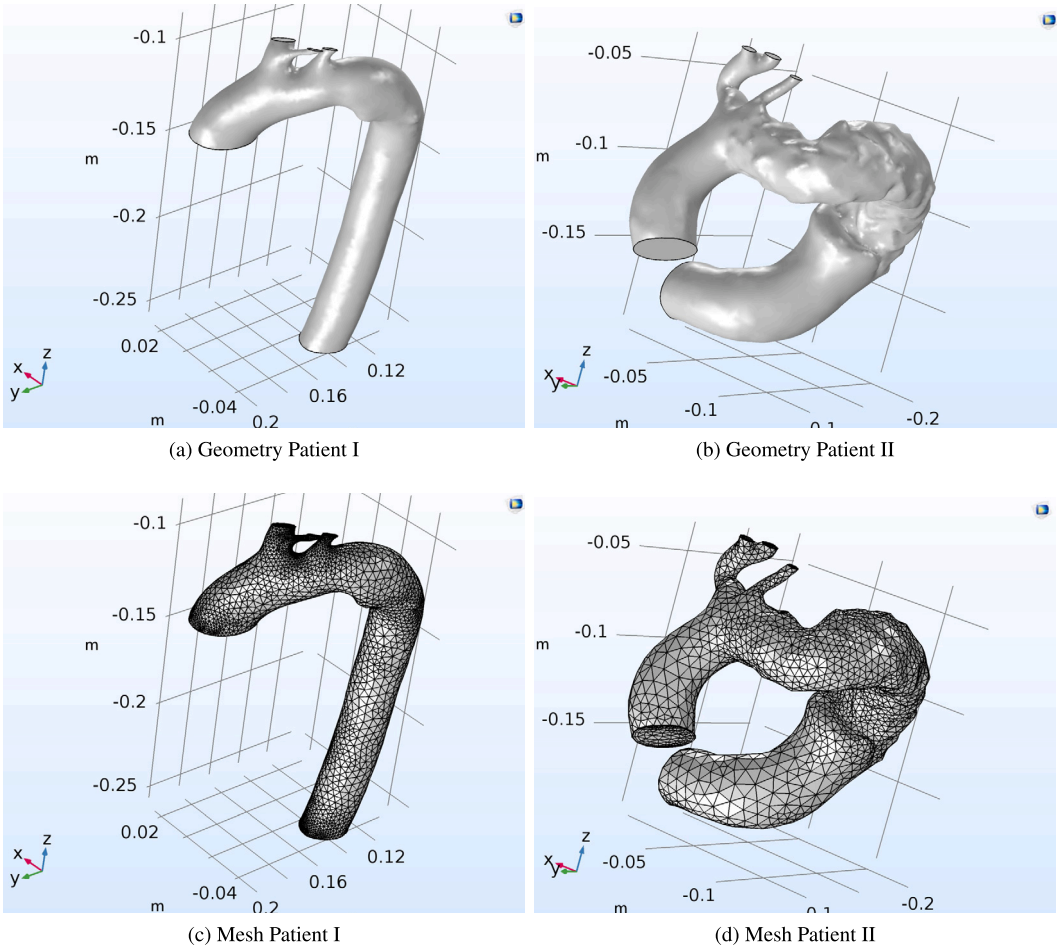

(a) Geometry Patient I (b) Geometry Patient II

(c) Mesh Patient I (d) Mesh Patient II

Fig. 3. Geometries and meshes of the aortas of Patients I and II.

$$\nabla . U = 0 \tag{2}$$

where U is the velocity (m/s); P is the pressure, which corresponds to a Lagrange multiplier to satisfy the incomprehensibility condition (Pa, or $mmHg$); μ is fluid viscosity ($N \times s/m^2$ or $Pa \times s$); and ρ: liquid density (kg/m^3). For the case of the cardiovascular system, where blood is considered an incompressible fluid (blood density is constant in space and time), the Equation (2) is zero [34]. The Equation (1) represents the parameters that influence the behavior of the fluid, whereas the Equation (2) establishes the continuity equation.

The Navier-Stokes equations for momentum and mass conservation, which govern fluid motion, are solved using the Finite Elements Method. The numerical solution is obtained using the software Comsol Multiphysics, considering a series of assumptions that parameterize the model, all of which are derived from previous studies mentioned below.

The blood is considered as an incompressible, homogeneous, and Newtonian fluid, which is a valid assumption in larger arteries with constant density value $\rho = 1060\ kg/m^3$ and constant dynamic viscosity $\mu = 0.0035\ Pa \times s$ [35], [33], [36], [30], [27], [12], [37] [38].

The vessel walls are considered to be rigid, and a no-slip condition is applied at the walls. A generic and idealized input waveform, representing the pulsatile velocity profile and not containing patient-specific flow characteristics, such as heart rate and systolic volume, is used as the initial condition [39]. Likewise, a shape of the pulsatile pressure waveform at the aortic outlets has been used and confirmed by various works (Figs. 4(a) and (b)) [40], [41], [35], [42], [43], [44], [45], [28].

The meshing process for both geometries is chosen to be unstructured, composed of tetrahedra, pyramids, and quadrilaterals, which are configured by the Comsol Multiphysics software itself according to the aortic anatomy, as shown in Figs. 3(c) and (d). To ensure that the simulation results are independent of the mesh, the mesh sizes were empirically tested. Normal and fine sizes, inherent to the Comsol software, were selected, taking into account the need to mitigate time-consuming aspects of transient simulations [39], as well as supported by the work of other authors [46], [43]. In this way, for Patient I, the maximum element size is 4.69 mm, and the minimum element size is 0.884 mm, with a total of 445,348 elements. For Patient II, the maximum element size is 9.14 mm, and the minimum element size is 2.73 mm, with a total of 216,702 elements.

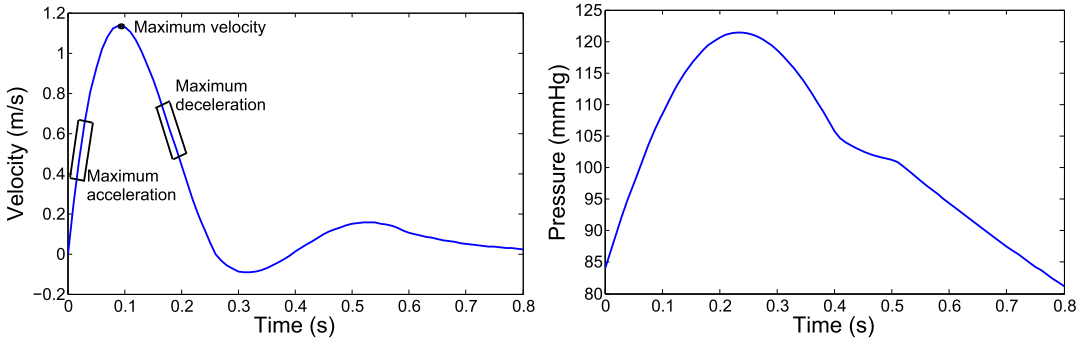

(a) Velocity (b) Pressure

Fig. 4. Initial and boundary conditions in aorta geometry.

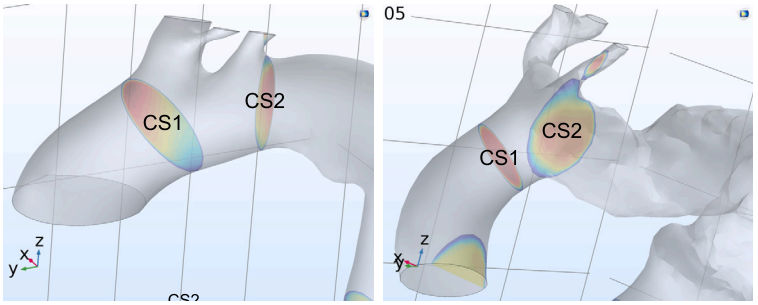

(a) Patient I (b) Patient II

Fig. 5. Cross-sections 1 and 2 of Patients I and II.

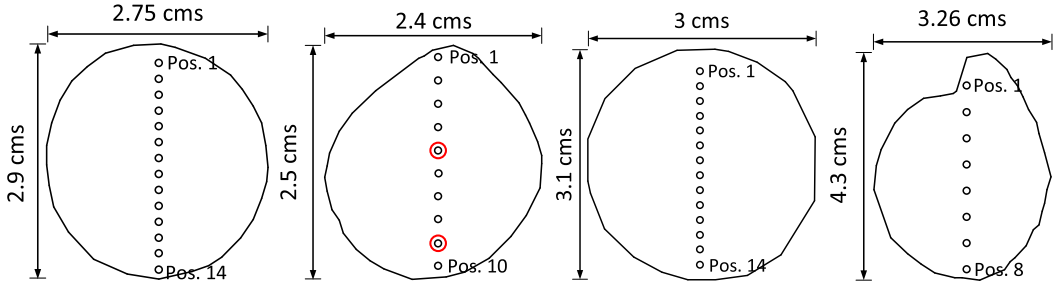

(a) (b) (c) (d)

Fig. 6. Geometry and dimensions to cross-sections. (a) CS1 - Patient I, (b) CS2 - Patient I, (c) CS1 - Patient II and (d) CS2 - Patient II.

A transient analysis is carried out for 3.2 s with a time step equal to 0.0032 s. Four cardiac cycles were simulated, with last around 0.8 s per cycle.

4. Results

A study on blood flow behavior is conducted in two patients with cardiovascular diseases, one of whom has an endovascular prosthesis. Velocity profiles and pressure distributions are acquired from two cross sections of the thoracic aorta (CS1 and CS2), situated before and after the blood flow bifurcations, as illustrated in Figs. 5(a) and (b). The location of CS1 is chosen before the fluid bifurcation to ensure that, even when the aortic conduit does not exhibit morphological alterations, the fluid does not respond to unpredictable hemodynamic variations. The positioning of CS2 serves the purpose of understanding the flow patterns after the fluid bifurcation, specifically to discern any differences and assess the potential influence of CS2 in Patient II. Notably, CS2 coincides with the proximal edge of the endoprosthesis.

The selection of measurement positions was based on the 3D geometry of the aorta for each patient, taking into consideration the anatomical orientation of the human body, as depicted in Figs. 6(a)-(d). Consequently, Position 1 (Pos. 1: Vel1 or Pres1) is situated in the upper arch or the internal concave zone of the aortic arch, while the final position is located in the lower arch or the convex

Table 1
Maximum errors in the time instants and in the selected positions.

	Time (s)		Max. Error		Time (s)		Max. Error	Position	Max. Error
ID	Cycle 2	Cycle 3	%	ID	Cycle 2	Cycle 3	%		%
1	0.80	1.60	0.89	8	1.11	1.91	0.44	Pos. 1	1.53
2	0.81	1.61	1.53	9	1.14	1.94	0.55	Pos. 2	0.55
3	0.87	1.67	0.06	10	1.20	2.00	1.72	Pos. 3	0.55
4	0.90	1.70	0.06	11	1.34	2.14	0.12	Pos. 4	0.68
5	0.93	1.73	0.06	12	1.50	2.30	0.27	Pos. 5	0.56
6	1.05	1.85	0.19	13	1.59	2.39	0.41	Pos. 6	0.92
7	1.08	1.88	0.38	14	1.60	2.40	1.67	Pos. 7	1.72
								Pos. 8	1.67

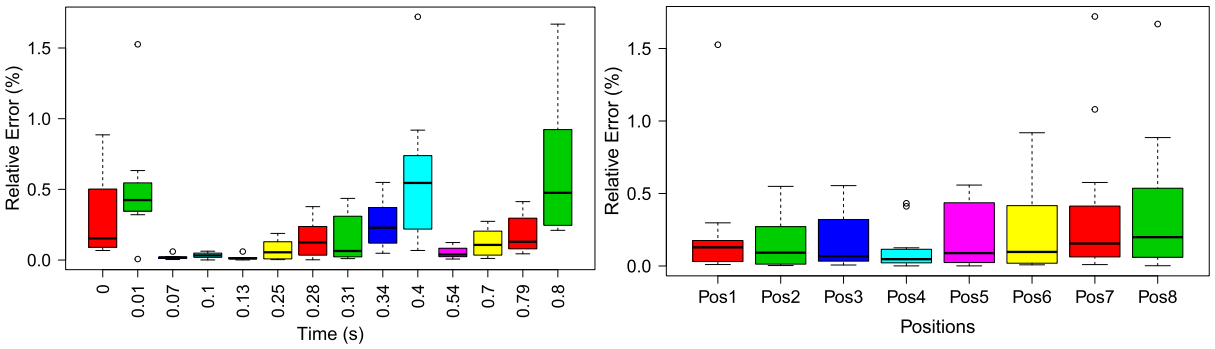

Fig. 7. Box-Plots relative error in CS2, Patient II. (a) Time, (b) position.

Table 2
Samples number to velocity and pressure.

	Patient I				Patient II			
	Cross-Section 1		Cross-Section 2		Cross-Section 1		Cross-Section 2	
	Velocity	Pressure	Velocity	Pressure	Velocity	Pressure	Velocity	Pressure
Position	14	14	10	10	14	14	8	8
Time	14	15	14	15	14	15	14	15
Total	196	210	140	150	196	210	112	120

zone of the aortic arch. The simulation spans four cardiac cycles, with each cycle lasting 0.8 s. The model initiates with a transient phase that stabilizes by the end of the first cycle, achieving regularity and repeatability in the measurements of velocity and pressure waves.

To confirm the stability, velocity magnitudes from cardiac cycles 2 and 3, corresponding to CS2 in Patient II, are considered. Pressure magnitudes are not utilized due to their less significant variations between cycles. CS2 in Patient II is selected because it exhibits the greatest variability in magnitudes, owing to its location at the fluid bifurcation's edge and its unique geometry, influenced by an aneurysm and subsequent repair with an endovascular prosthesis.

The relative error is utilized as a metric, with reference to the velocity magnitudes of Cycle 3 in relation to Cycle 2. The maximum errors are computed at 14 time points throughout the cardiac cycle and at the eight positions of CS2, as presented in Table 1. It is noted that the highest error, 1.7%, is followed closely by 1.5%. However, these two particular cases are primarily influenced by two factors: firstly, the proximity of the measurement position to the fluid bifurcation and the edges of the modified aortic geometry; and secondly, their occurrence during the initial or final stages of the cardiac cycle and immediately after the phase transition from systole to diastole. During this transition, alterations in the measurements are induced by retrograde flow. Two Box-Plots have been created to better comprehend the behavior of relative error at all time points and positions. One of them displays errors by time instant (Fig. 7(a)), while the other presents errors by position (Fig. 7(b)). These plots reveal that the error percentage remains largely below 0.5% (constituting 91.1% of the total errors), with the previously mentioned maximum errors identified as outliers in the Box-Plots. Consequently, the maximum variation in velocity observed during the calculations did not exceed 0.5% between the second and third cycles. This aligns with findings reported in [43] and [45].

For this reason, the results and subsequent analysis are based on measurements taken during the third cardiac cycle (from 1.6 s to 2.4 s), at the specific number of positions and time points listed in Table 2. Considering the information above, the analysis of velocity profiles and pressure distributions is conducted based on the measurements of their magnitudes and the interpretation of

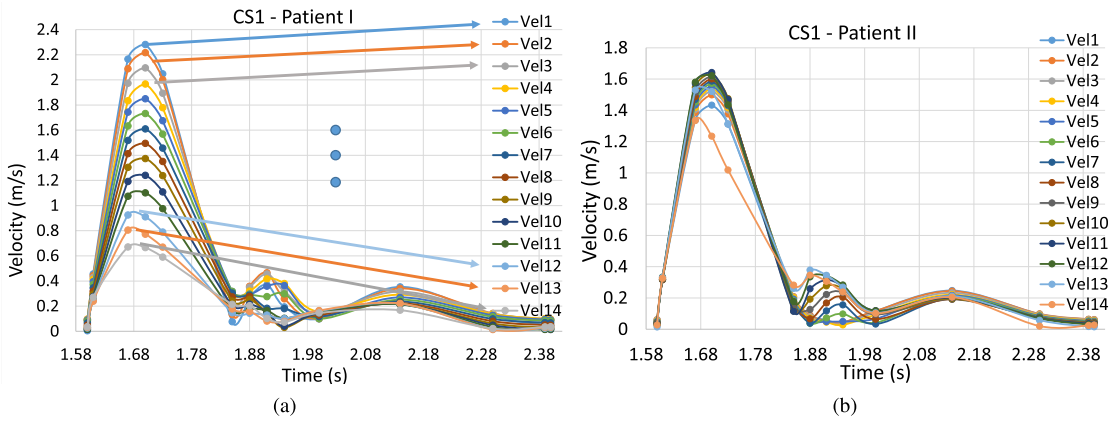

Fig. 8. Velocity waveforms in CS1. (a) Patients I, (b) Patient II.

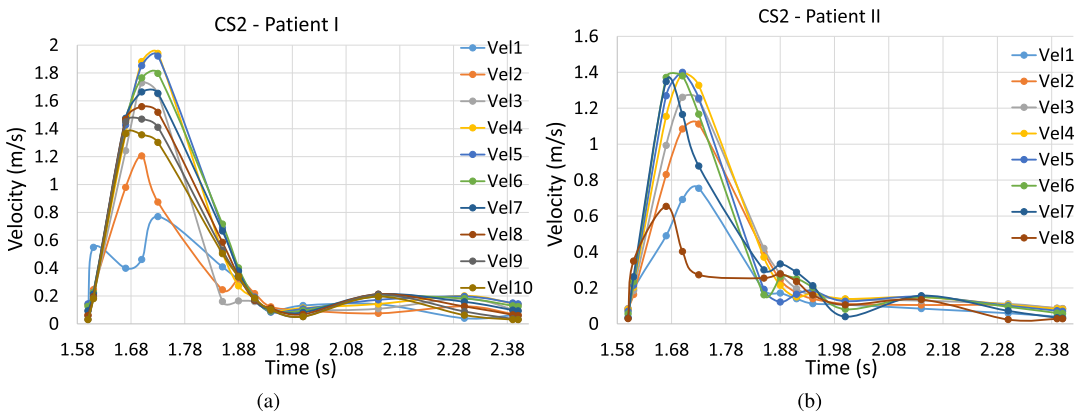

Fig. 9. Velocity waveforms in CS2. (a) Patient I, (b) Patient II.

waveforms represented in a 2D plane. The abscissa axis corresponds to time, while the ordinate axis represents the magnitude value of the measured variable (velocity or pressure). This graphical representation proves valuable in understanding the response of the blood flow model in the aorta and at the predefined positions for each cross-section, with initial conditions configured as velocity and pressure trajectories (Fig. 4).

As shown in Figs. 6(b) and (d), the number of positions in Patient I CS2 (10) does not match that of Patient II CS2 (8). However, based on the results below, it becomes evident that the measurements taken at Positions 5 and 9 of Patient I (Fig. 6(b)) closely resemble both numerically and graphically those of Positions 6 and 10, respectively. The differences at Position 5 are minimal, and the maximum changes are only 0.3 $mmHg$ and 0.1 m/s at Position 9. Consequently, whether or not these positions are included does not affect the conclusions drawn from the analysis.

As a complement to the analysis of the results, Box-Plots are used to measure the dispersion of the velocity and pressure magnitudes at each time instant according to the measurement positions.

Analysis of the Behavior of Waves Representing the Velocity Profiles: It is evident in Figs. 8 and 9 that notable changes occur in the waveforms from one position to another. These differences are particularly pronounced at time instants within the region where acceleration and deceleration are at their maximum, and where the highest peak velocity is reached (Fig. 4(a)). These variations in the waveforms are attributed to the instability of hemodynamic phenomena within the major vessels and the curvature of the aorta, a condition that is clearly evident in the patients under study, as reported by [47]. On the other hand, it is observed that the velocity magnitudes in the aortic geometry of Patient I exceed those of Patient II. In contrast, the pressure magnitudes in Patient I are lower compared to Patient II. This behavior is attributed not only to the shorter distance the fluid travels in Patient I but also to the larger diameter of the arteries in Patient II.

It is also evident that at time instants 1.67 s, 1.7 s, and 1.73 s, as shown in Fig. 8(a), corresponding to the intermediate phase of systole, the velocity magnitude in CS1 of Patient I experiences a rapid and nearly constant decrease. This decrease maintains a value of $0.1171 \pm 0.026 m/s$ for each of the positions, starting at Position 1 and ending at Position 14. In contrast, for Patient II during the same intermediate phase of systole, the velocity magnitude curves are highly similar to each other, with the exception of the curve at Position 14 (Fig. 8(b)).

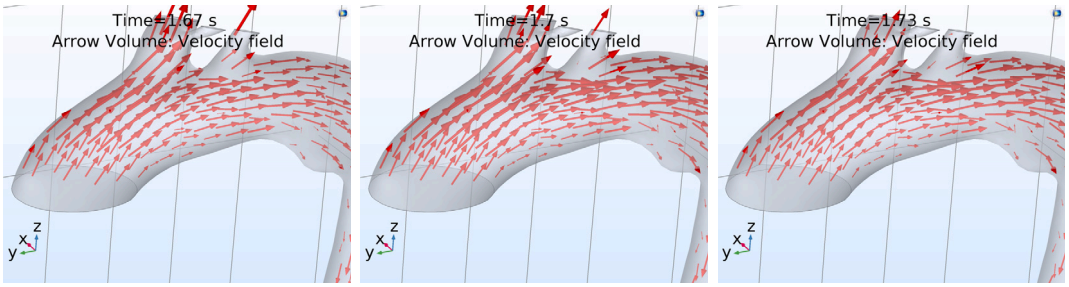

(a) (b) (c)

Fig. 10. Arrow volume: velocity field of the systole - Patient I.

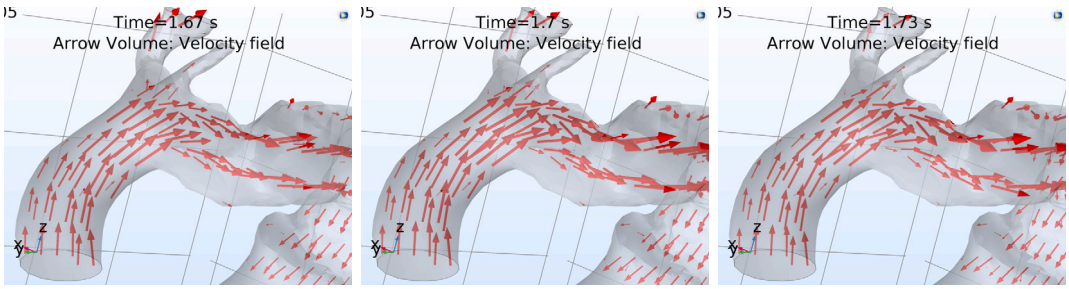

(a) (b) (c)

Fig. 11. Arrow volume: velocity field of the systole - Patient II.

This velocity behavior observed in CS1 of Patient I can be attributed to the initial direction taken by the fluid as it enters the aorta, as illustrated by the velocity vectors in Figs. 10(a)-(c). These vectors directly collide in substantial numbers with the upper wall or concave zone of the duct, resulting in high blood flow velocities, contrasting with the situation in the convex zone. This contrast is more pronounced in Patient II due to the fluid having traveled a greater distance from the inlet to CS1, coupled with the geometry of the aortic conduit. This distribution of velocity vectors is more uniform throughout the region, as shown in Figs. 11(a)-(c). The velocity waveforms in CS2 of the two patients, as shown in Fig. 9(a) and (b), exhibit distinct behaviors, deviating from their original patterns, with a significant disparity, particularly in the first two positions. These positions are situated in close proximity to the entrance of the left subclavian artery, where the fluid undergoes bifurcation. In this region of separation, flows with varying quantities of motion interact in different directions due to the channel orientations that form the bifurcation, leading to the formation of vortices, as discussed in [48].

Furthermore, in the case of Patient II, CS2 coincides with the proximal edge of the endoprosthesis. This proximity accentuates the alterations in velocity profiles, especially those generated in the vicinity of the edges (Positions 1, 2, 7, and 8).

These results begin to confirm the influence of the proximal edge of the endovascular prosthesis on blood flow behavior in a real aorta model obtained through CT image processing of a specific patient. The significance of this influence becomes even more evident in the subsequent results, which are of great clinical interest.

Analyzing Pressure Distribution Wave Behavior: In the systole phase of both patients, small variations in blood pressure magnitudes are observed (Figs. 12(a) and (b) and Figs. 13(a) and (b)). These variations become more pronounced and clinically relevant in CS2. However, during the diastole phase, no significant pressure variations are noticeable in any of the positions.

In CS2 of Patient I, the highest pressure magnitudes occur at the time instant of 1.64 s, just before reaching the maximum velocity (1.7 s). Nonetheless, the pressure differential is low at this point, only 2%, with a maximum pressure of 126.3 $mmHg$. When the velocity reaches its maximum, there is a pressure differential of 10.9% with only two pressure values (124 mmH and 121 $mmHg$) exceeding the baseline pressure of 120 $mmHg$. However, this differential is not a clinical concern as it is near the fluid bifurcation, where natural flow alterations also affect pressure. By the next time instant of 1.76 s, the pressure differential drops to 2%. These results are indicated in the highlighted region of the waveforms in Fig. 13(a).

In CS2 of Patient II, a substantial presence of pressure differentials is observed during the systole phase: 4% at 1.64 s, 10% at 1.7 s, 6.1% at 1.76 s, and 3.6% at 1.79 s, as shown in the boxed area of the waveforms in Fig. 13(b). The maximum and minimum magnitude values are respectively 131.3 $mmHg$ and 119.5 $mmHg$, occurring at the instant of maximum velocity. These differentials are consistently located near the proximal anchor zone of the endovascular prosthesis. The significance of these differentials lies in the fact that, when multiplied by the heartbeat frequency, they can lead to asymmetries at the ends of the endoprosthesis and an increase in shear forces. The consequences may include anatomical deformation, potentially impeding the correct anchorage of the prosthesis and leading to subsequent displacement.

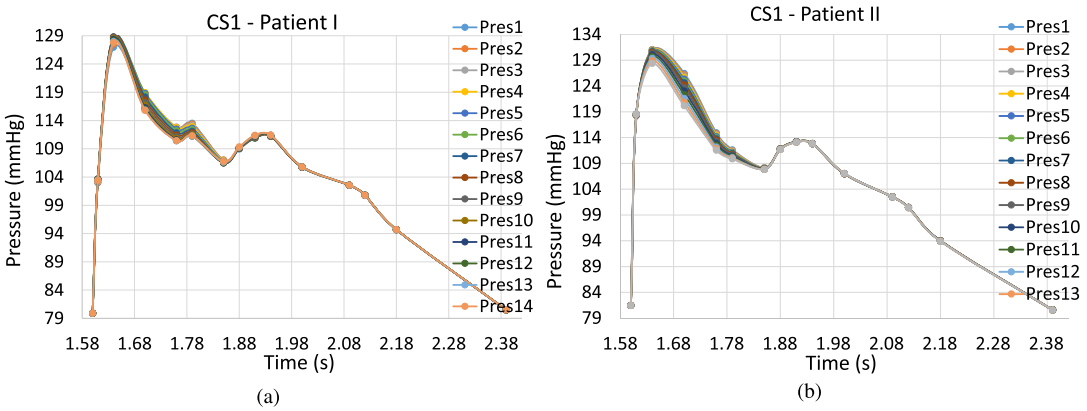

Fig. 12. Pressure waveforms in CS1 of patients I and II.

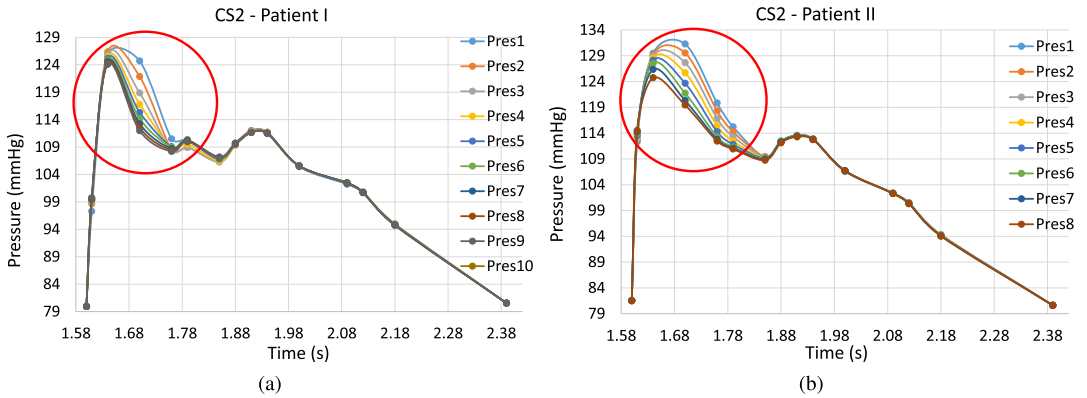

Fig. 13. Pressure waveforms in CS2 of patients I and II.

Table 3
Extrapolation of the measurement time instants of cycle 3 to the base cycle.

Velocity				Pressure			
Time (s)		Time (s)		Time (s)		Time (s)	
Cycle 1	Cycle 3	Cycle 1	Cycle 3	Cycle 1	Cycle 3	Cycle 1	Cycle 3
0.00	1.60	0.31	1.91	0.00	1.60	0.31	1.91
0.01	1.61	0.34	1.94	0.01	1.61	0.40	1.94
0.07	1.67	0.40	2.00	0.04	1.64	0.49	2.00
0.10	1.70	0.54	2.14	0.10	1.70	0.52	2.09
0.13	1.73	0.70	2.30	0.16	1.76	0.58	2.12
0.25	1.85	0.79	2.39	0.19	1.79	0.79	2.18
0.28	1.88	0.80	2.40	0.25	1.85	0.80	2.39
				0.28	1.88		

4.1. Box-Plot analysis

Statistical analysis is conducted using Box-Plots for each patient and cross-section. The time axis in the Box-Plots is transformed to the typical duration of a cardiac cycle (base cycle: 0.0 s to 0.8 s). This transformation is performed to facilitate a simpler and quicker interpretation when associating the times with the duration of the systolic and diastolic phases of the cardiac cycle, as detailed in Table 3.

Cross-Section 1 - Patient I and Patient II: In the Box-Plot diagrams in Fig. 14(a), we observe a low dispersion of velocity magnitudes during the initial two time instants. However, as we move from 0.07 s to 0.13 s, which corresponds to the intermediate phase of systole, the dispersion rapidly increases, reaching its peak at 0.1 s, coinciding with the moment of maximum velocity (1.75 s in the third cardiac cycle).

Despite the data dispersion, an almost symmetrical distribution is maintained, with a mean very close to the median. Subsequently, the dispersion decreases rapidly, but a slight dispersion reappears in the time interval from 0.25 s to 0.34 s. This dispersion is mainly

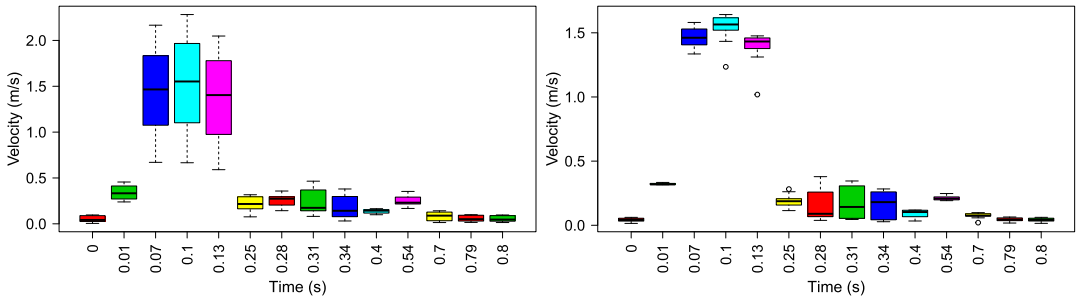

(a) Velocity - Time, CS1 Patient I (b) Velocity - Time, CS1 Patient II

Fig. 14. Box-Plots CS1 - Patients I and II.

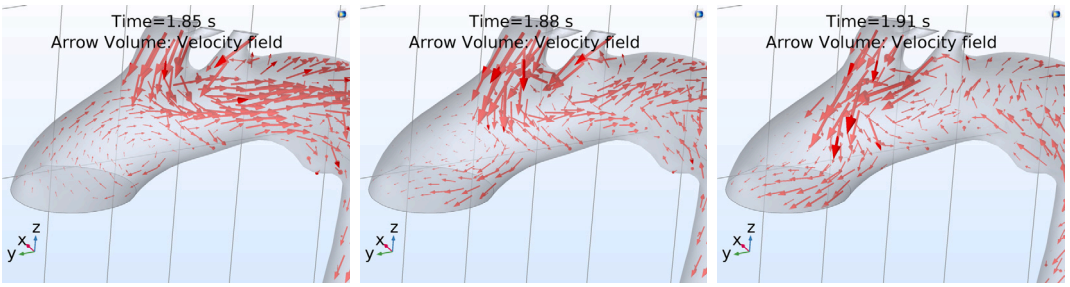

(a) (b) (c)

Fig. 15. Arrow volume: velocity field of retrograde flow - Patient I.

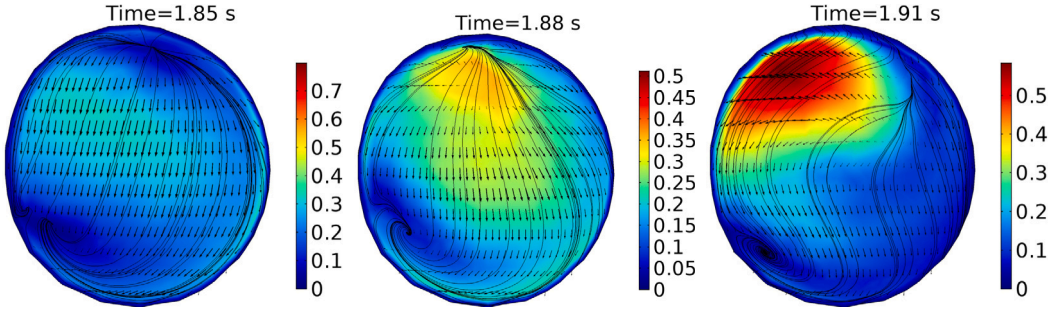

(a) (b) (c)

Fig. 16. Streamlines in Cross-section 1 for Patient I.

caused by the measurement positions and the presence of retrograde flow, evident in the change of direction of the velocity vectors, as shown in Figs. 15(a)-(c), and the effect of vortex formation, as indicated by the streamlines in Figs. 16(a)-(c).

During the systole phase, and reinforcing the earlier discussion, Figs. 10(a)-(c) illustrates how the magnitude of velocity vectors extends more widely and gathers in greater quantity on the concave surface of the aorta, resulting in higher velocities. In contrast, a smaller grouping of shorter velocity vectors is observed on the convex surface of the aorta, associated with lower velocities. However, for Patient II, in contrast to Patient I, the Box-Plots in Fig. 14(b) during the intermediate phase of systole indicate a smaller dispersion. They maintain a symmetrical distribution with minimal differences between quartile ranges. It is in the later time instants, spanning from 0.25 s to 0.4 s, where we observe a more noticeable scatter in velocity magnitudes. During this interval, the data distribution lacks uniformity, primarily due to the presence of retrograde flow, which significantly affects fluid behavior. This flow is clearly represented in the velocity vectors shown in Figs. 17(a)-(c) and the streamlines in Figs. 18(a)-(c).

Cross-Section 2 - Patient I and Patient II: In the case of Patient I, the Box-Plots in Fig. 19(a) reveal that data dispersion becomes noticeable at 0.07 s and continues to increase rapidly and almost linearly until it reaches its maximum value, which is slightly more than twice the initial Box-Plot range. This occurs at 0.13 s, coinciding with the moment of maximum velocity. It is worth noting that there is a small difference of 0.03 s from the time when the maximum velocity occurs in the initial model conditions, a unique characteristic for this cross-section.

The outliers in the Box-Plots are linked to measurements taken near the cross-section edges and in proximity to the subclavian-artery proximal area. Although the scatter decreases at 0.25 s, it remains noticeable due to the onset of retrograde flow caused by

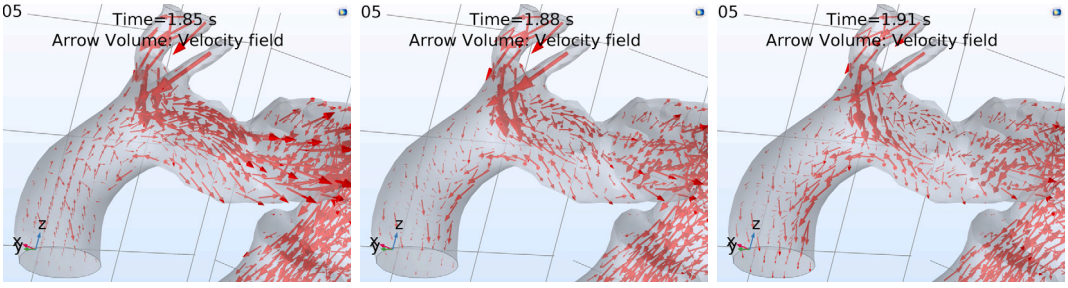

Fig. 17. Arrow volume: velocity field of retrograde flow - Patient II.

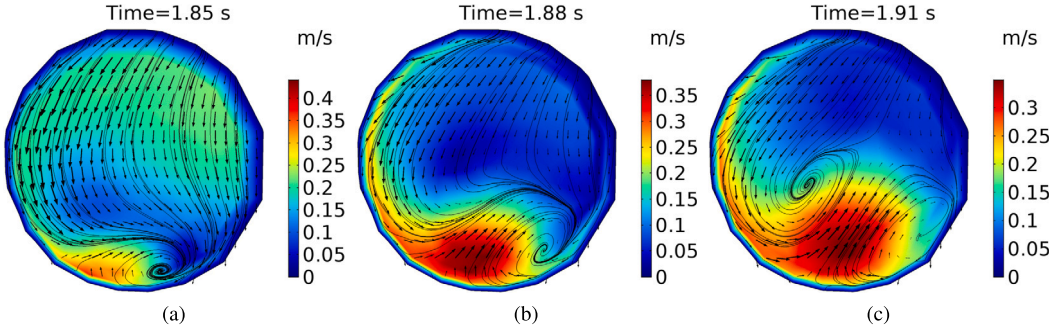

Fig. 18. Streamlines in Cross-section 1 for Patient II.

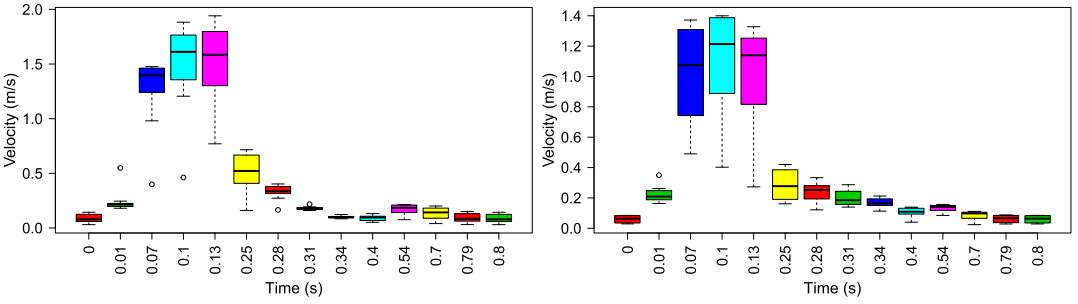

Fig. 19. Box-Plots CS2 - Patients I and II.

changes in pressure and a sharp decline in velocity. This behavior is visually evident in the magnitude and direction of velocity vectors as shown in Figs. 15(a)-(c) and in the streamlines with vortex formation displayed in Figs. 20(a)-(c). In the case of Patient II, the Box-Plot plots in Fig. 19(b) once again reveal a significant scatter of velocity magnitudes, resembling what was observed in CS1 for Patient I. However, the distribution of values between quartiles changes at each of the time instants with high velocities (at 0.07 s, 0.1 s, and 0.13 s). Similar to Patient I (CS2), a minor dispersion occurs at the time instant of 0.25 s due to the retrograde flow, which can be visualized in the flow vectors and streamlines presented in Figs. 17(a)-(c) and Figs. 21(a)-(c), respectively.

It's worth emphasizing that CS2, in addition to being located at the border of the subclavian artery, coincides with the proximal zone of the prosthesis. As shown in Fig. 6(d), its irregular geometry further influences the velocity profiles throughout the analyzed region. Regarding pressure in CS1 for both patients, the Box-Plot diagrams in Figs. 22(a) and (b) allow us to observe slight dispersions that are barely noticeable in the curves in Figs. 12(a) and (b). These dispersions occur during the systole phase and at the time instants of 0.1 s, 0.16 s, and 0.19 s, with the most noticeable one happening at the moment of maximum velocity (0.1 s). However, there are no significant changes in the pressure differentials that justify further analysis. In CS2 of Patient I, the Box-Plots in Fig. 23(a) reveal a notable dispersion in pressure magnitude values at the time instant of 0.1 seconds. This dispersion is closely linked to changes in blood flow resulting from the proximity of the cross-section to the fluid bifurcation.

However, in CS2 of Patient II (Fig. 23(b)), the scatter extends through almost the entire systole phase and is not solely related to the fluid bifurcation. It is primarily due to the cross-section's alignment with the proximal part of the endoprosthesis. As previously mentioned, the irregular geometry resulting from the prosthesis-endothelium junction alters blood flow, resulting in

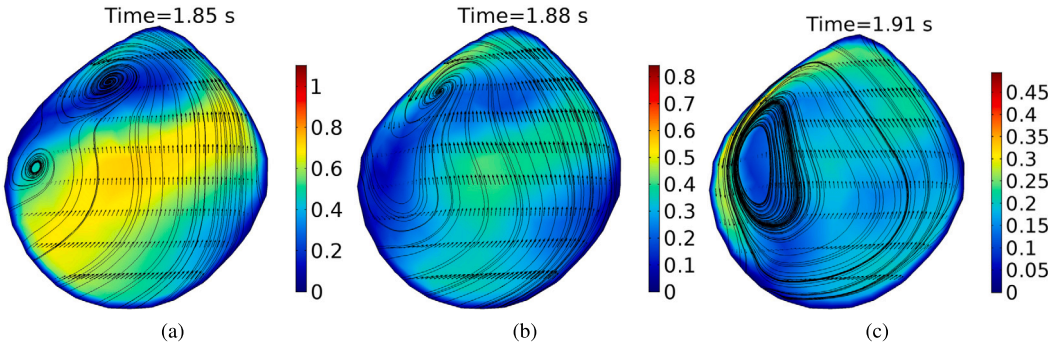

Fig. 20. Streamlines in Cross-section 2 for Patient I.

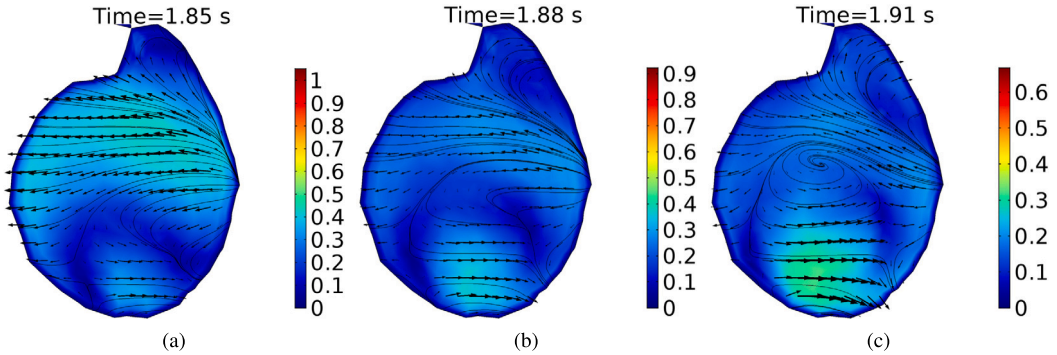

Fig. 21. Streamlines in Cross-section 2 for Patient II.

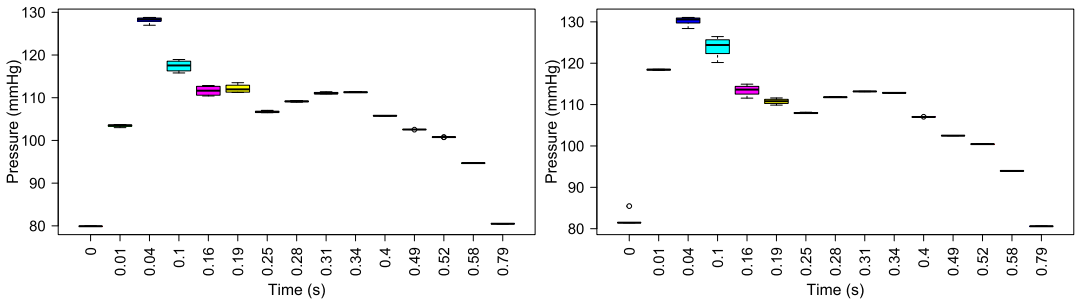

(a) Pressure - Time, CS1 Patient I (b) Pressure - Time, CS1 Patient II

Fig. 22. Box-Plots CS1 - Patients I and II.

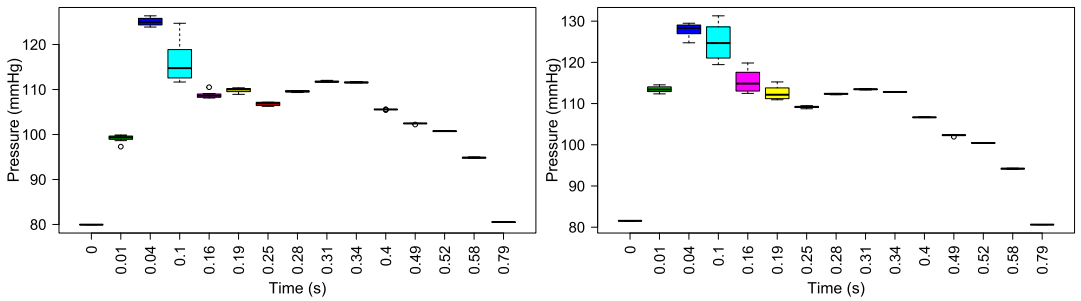

(a) Pressure - Time, CS2 Patient I (b) Pressure - Time, CS2 Patient II

Fig. 23. Box-Plots CS2 - Patients I and II.

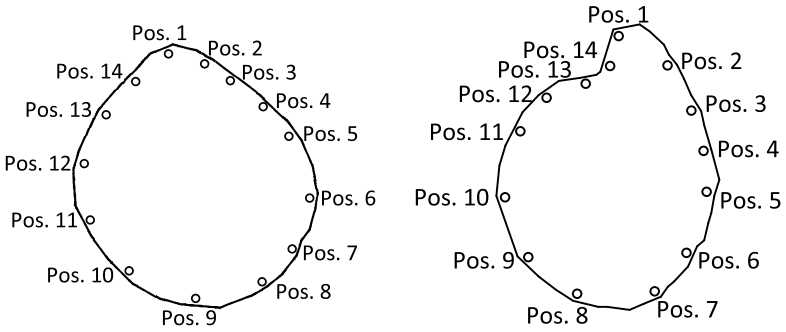

Fig. 24. Measurement positions in CS 2 - Patients I and II.

pressure differentials that reach and exceed 10% of their nominal values. These differentials can be transmitted to the ends of the endoprosthesis, creating forces that have the potential to alter the anatomy, leading to prosthesis migration or disruption of the prosthesis-endothelium continuity. The maximum differential remains particularly prominent at the time instant of $0.1\ s$. At other time instants, there is a higher degree of regularity, which becomes more pronounced during the diastole phase. During this phase, the pressure magnitudes in both patients closely resemble patterns commonly observed in the work reported by other authors and in aortic geometries similar to those of the two patients under study.

All these alterations in blood flow, including variations in velocity and pressure, are detected in specific regions and time intervals. They are most pronounced in CS2 of Patient II due to the proximity of the fluid to the proximal area of the endovascular prosthesis. In this region, rheological phenomena lead to the formation of vortices and the emergence of pressure differentials. When combined with the continuous beating of the heart, these factors can result in partial detachment of the prosthesis, causing irreparable damage to the region of the proximal anchorage of the endoprosthesis.

The analysis of Wall Shear Stress (WSS) is added to reinforce the findings provided by the results of velocity and pressure magnitudes, a variable directly related to the propensity for substance accumulation on the arterial wall. There is evidence that associates the WSS distribution factor with the vascular disease known as atherosclerosis [49], and it is currently considered an effective metric for the early diagnosis of atherosclerosis [50].

4.2. Analyzing WSS represented wave behavior

The study now shifts its focus exclusively to CS2 to confirm the WSS patterns and after analyzing the magnitudes of velocity profiles and pressure distributions in the two cross-sectional areas of both patients, as alterations in flow patterns have been observed.

The study commences by selecting 14 positions, as depicted in Figs. 24(a) and (b), encompassing the majority of the cross-sectional area's perimeter. Similarly, 14 time instants were chosen, following the same approach used for velocity and pressure. This results in 196 values of WSS magnitudes for each patient, obtained by measuring at the 14 positions and at 14 time instants. The waveforms resulting from the measurements taken at a specific position and during one cardiac cycle are plotted, starting at $1.6\ s$ (the beginning of the third cardiac cycle) and ending at $2.39\ s$ (the completion of the third cardiac cycle). Subsequently, Box-Plots are constructed, and the results are analyzed, considering that low shear stress reduces endothelial production of nitric oxide and antioxidant proteins, which is related to the generation and progression of atherosclerotic plaques in the coronary, carotid, and aortic areas [51].

Regions characterized by diminished shear stress levels, specifically below $12.6\ dynes/cm^2$ ($1.26\ Pa$), exhibit a substantial increase in atherosclerotic plaque formation and an expansion of the vascular area, indicative of positive vascular remodeling. Conversely, areas experiencing shear stress, within the physiological range of 12.6 to 26.9 $dynes/cm^2$ (1.26 to 2.69 Pa), display no statistically significant alterations. Furthermore, regions subjected to elevated shear stress levels exceeding 27 $dynes/cm^2$ (2.7 Pa) demonstrate favorable arterial remodeling, with no concurrent modifications in the atheroma plaque [51].

One parameter related to WSS is the time-averaged value over the cardiac cycle, known as TAWSS (Time Average WSS), which is helpful for pulsatile flow types. In the human arterial system, TAWSS has an approximate value of $1.5\ Pa$ and values above have a protective effect while those below may result in a risk of plaque growth due to Intimal Hyperplasia (HI) [52].

The analysis of WSS results is focused on the systolic phase and the time interval where the systole-to-diastole transition occurs. In this way, the graphs shown, divided into four groups (Figs. 25), aim to classify, into sets or regions, the positions along the perimeter of the cross-sectional area where similar WSS magnitudes are generated. As can be observed, the highest WSS values are found at Position 1 and Position 14 (Fig. 25(a)), with maximum values of $12.7\ Pa$ and $15.1\ Pa$, which are lower than those in other considered works to be capable of triggering platelet activation and the formation of microparticles, their accumulation, and subsequent rupture of the atherosclerotic plaque [52], [53]. Following, there are Positions 5, 6, 7, 8, 9, and Position 12 (Fig. 25(c)), whose waveforms are more regular and follow the flow velocity pattern for both the systolic and diastolic phases, with maximum magnitude values ranging from $6\ Pa$ to $8.5\ Pa$.

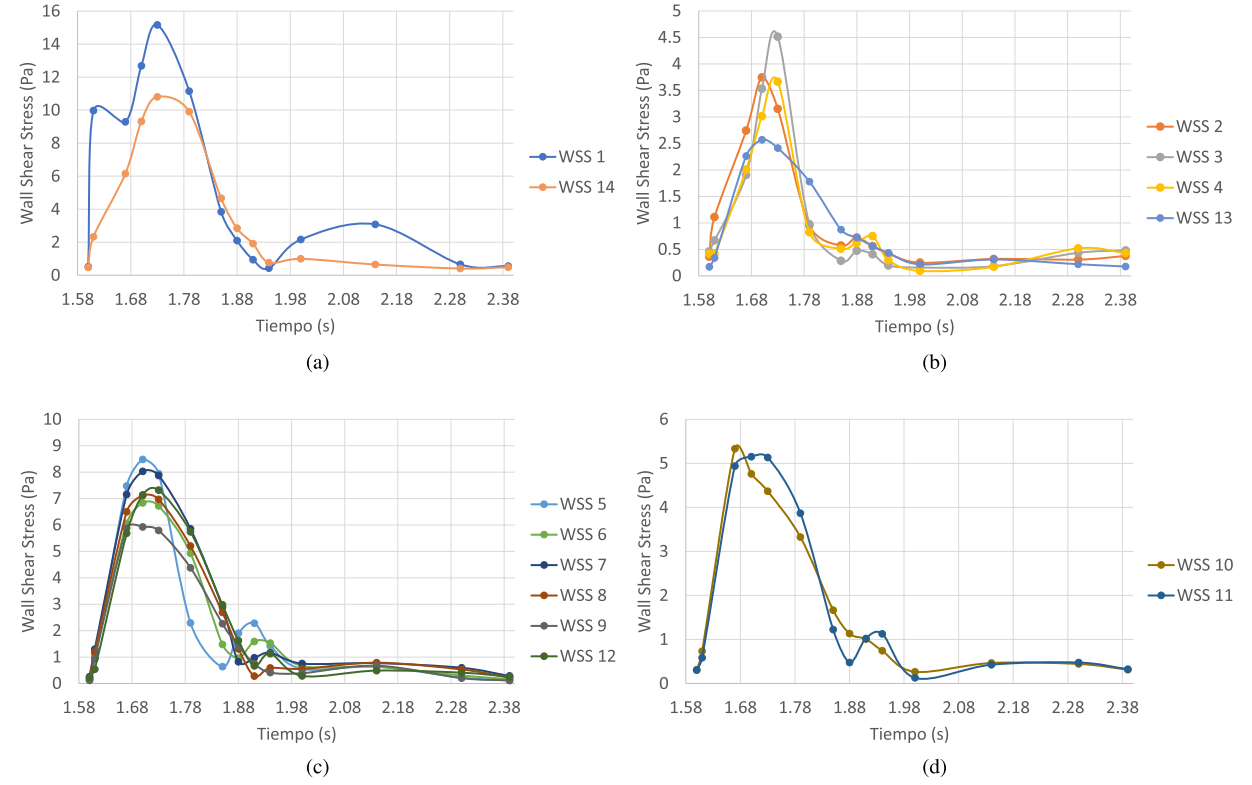

Fig. 25. WSS waveforms in CS2 to Patient I.

In Fig. 25(d), the waveforms correspond to Positions 10 and 11, with slightly lower magnitude values (5.2 Pa and 5.3 Pa) compared to the positions mentioned before. Finally, in Fig. 25(b), the shear stress magnitudes with the lowest values are shown, but they are not within the range considered risky for the patient under study (between 2.5 Pa and 4.5 Pa). These values are associated with Positions 2, 3, 4, and Positions 13.

Similarly, for Patient II, the graphs are grouped following the same considerations (Figs. 26). The difference here is that low WSS values are presented, which are, therefore, the subject of analysis. As previously mentioned, the effects of low-shear stress favor plaque progression and influence the development of atherosclerotic disease [51]. Even though the appearance of the graphs is grouped in nearly consecutive order, starting from Position 1 to Position 14, the analysis begins with Fig. 26(e) considering that the maximum magnitudes in these positions (Positions 11 and 12) are the highest among all the waveforms, and their averages of 1.5 Pa and 1.3 Pa fall within the range where shear stress has a protective effect on the endothelium.

In Figs. 26(b), (d), and (f), a very similar behavior is observed in all the waveforms. However, they are grouped in different graphs to perceive these small differences better. In Fig. 26(b), the maximum values are between 2.5 Pa and 3 Pa. In Fig. 26(d), they range between 3 Pa and 3.5 Pa, and in Fig. 26(f), they range from 3.3 Pa to 3.8 Pa. Only at Position 8 is there fluctuating alteration after 1.8 s (0.2 s into the baseline cycle) when the retrograde flow is present. Additionally, the TAWSS values at each of the mentioned positions are practically at the lower threshold limit of 1 Pa, which is not sufficient reason to make a valid judgment.

It is important to note the behavior of Fig. 26(a). As observed, the maximum values of the two waveforms are around 1.2 Pa, with one above and the other below. However, the average value for Position 1 (WSS 1) is 0.5 Pa, and for Position 2 (WSS 2) is 0.42 Pa. These magnitudes indicate a progression of atherosclerotic plaques, negatively impacting the neointimal response to prosthesis implantation and consequently contributing to restenosis [51].

Finally, in Fig. 26(c), there is a fluctuation in WSS with maximum amplitudes of 2 Pa and 1.8 Pa at Positions 6 and 7, respectively. The TAWSS values are 0.7 Pa and 0.79 Pa, below the threshold and within the risky zone. In this regard, these two characteristics reaffirm the presence of rheological complications directly affecting the patient health.

WSS Analysis using Box-Plot Box-Plot diagrams are created to represent the distribution and dispersion of WSS values at each time instant to complement the interpretation and analysis of the data, as shown in Fig. 27(a)-(b). In Patient I (Fig. 27(a)), the shear stress values are within the range of physiological values considered normal. A few of them are slightly higher and are referred to as increased shear rate, meaning they have a protective effect on the endothelium [51], [54].

Similarly, the figures reflect that during the diastolic phase, due to the relaxation of the cardiac muscle, WSS falls below 1 Pa. This behavior is because WSS is directly related to changes in velocity, which are of small magnitude during this phase. This statement can be addressed and reinforced in future work. As is known, rheological changes occur during this last instant due to retrograde flow, contributing to the decrease in WSS.

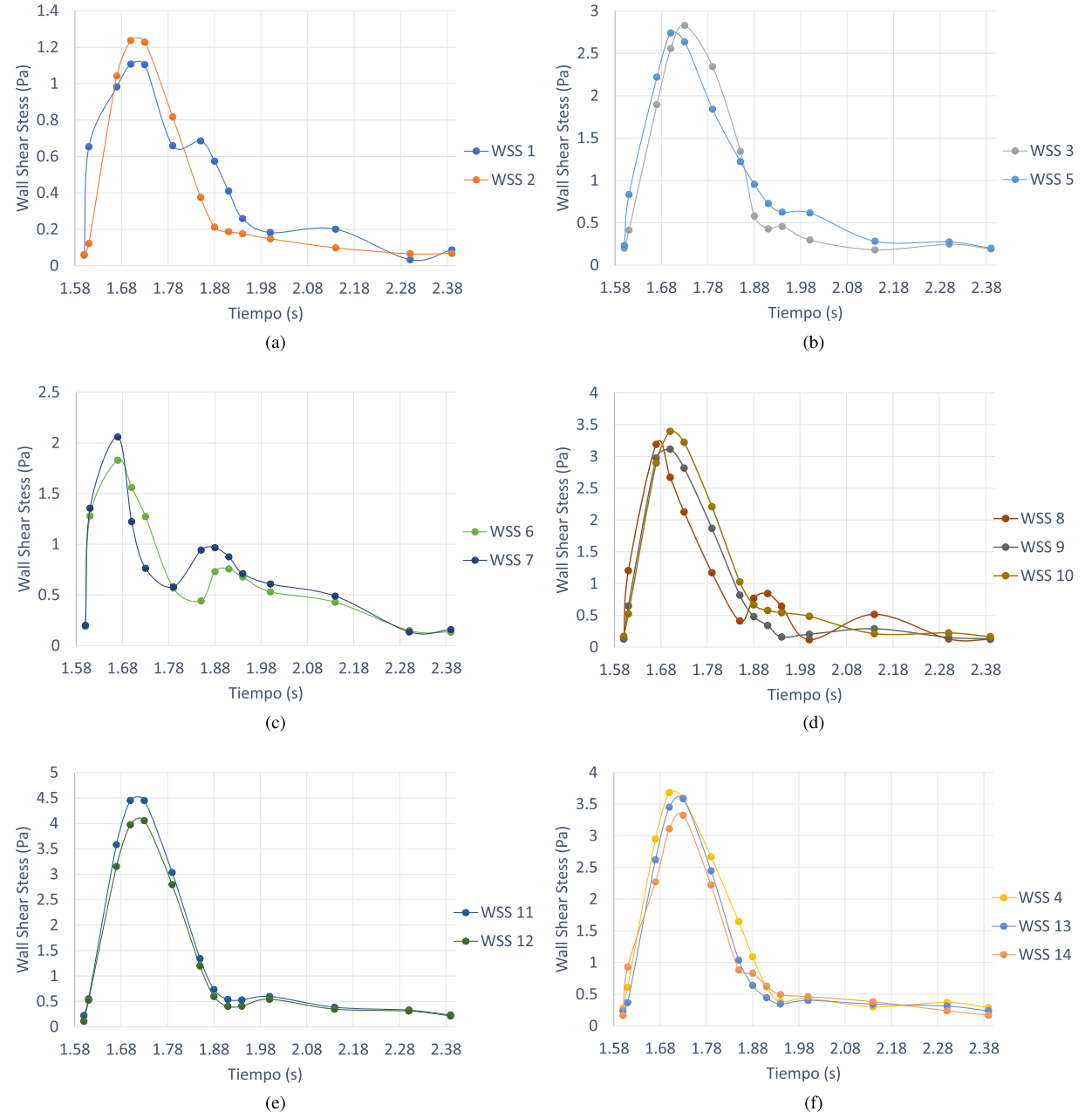

Fig. 26. WSS waveforms in CS2 to Patient II.

Similarly, for Patient I, the Box-Plot diagram in Fig. 27(a) shows a balance in the data distribution. Some spreads are more extensive than others, becoming further noticeable starting at 0.07 s, and predominating even more in the middle and end of the systolic phase. The larger spreads (from the third quartile to the final value) occur at the time when the velocity is maximum (0.1 s) and at the moment when the systole-to-diastole phase change begins due to the presence of retrograde flow. Outliers in the data, while not contributing much to the analysis, fall within the range of WSS values considered protective. At 0.1 s, 0.13 s, and 0.19 s, the highest WSS values coincide with the maximum velocity and pressure magnitudes at those time instants.

For Patient II, Fig. 27(b) reveals a notable decrease in WSS values compared to Patient I. Furthermore, the distribution and dispersion of the data are primarily below the median value, indicating that there are few WSS values above the threshold of vascular shear stress with a protective effect. As a result, the vascular risk increases. The highest median (2.93 Pa) and the highest WSS values occur when fluid velocity is at its maximum (0.1 s), highlighting that most WSS values at that moment are of small magnitude. This confirms that the values at other time instants are even smaller, as illustrated in Figs. 27(a) and (b).

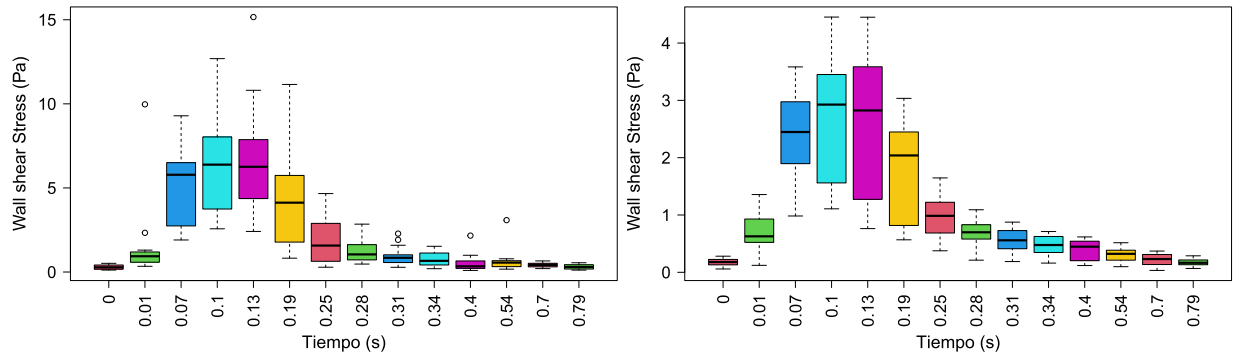

(a) Wall Shear Stress - Time, CS2 Patient I

(b) Wall Shear Stress - Time, CS2 Patient II

Fig. 27. Box-Plots CS2 - Patients I and II.

The mean TAWSS is calculated over a complete cardiac cycle, with the WSS magnitudes during the systolic phase emphasizing low values in the diastolic phase for a patient with some or no cardiovascular complications. However, increased shear stress predominates, as previously mentioned, exerting a protective effect on the vascular endothelium.

In the case of Patient II CS2, the WSS values concentrated in the systolic phase are not large enough to raise the mean vascular shear rate above the threshold considered to be free of the risk of causing vascular complications. Only at Position 11 and 12, TAWSS reaches 1.5 Pa and 1.3 Pa, respectively, just exceeding the protective effect threshold of 1.26 Pa, as demonstrated in the work of Stone et al. in [55].

Finally, local hemodynamic alterations following the implantation of endoprostheses, coupled with low shear stress, as detected in this study in the proximal region of the endovascular prosthesis, contribute to an increase in neointimal proliferation and, therefore, favor restenosis. Thus, simulation becomes a highly useful tool in medical practice for making timely and anticipatory decisions in diagnoses, ultimately benefiting the quality of life and health of the patients.

5. Conclusions

This paper presents a proof-of-concept, demonstrating the utility of simulation techniques for diagnosing issues arising from the use of endovascular prostheses. Specifically, the study focuses on the hemodynamic effects at the proximal edge of the prosthesis by processing images obtained from two patients, one of whom has undergone endovascular repair.

The results highlight differences primarily attributed to the geometric structure of the region of interest (ROI). While blood flow behavior can be influenced by geometric variations in the conduit, these responses will be patient-specific, adhering to the principles of fluid dynamics, with a somewhat predictable pattern. However, irregularities in the geometry, where some of the measurements (CS2) were obtained from the patient with an endoprosthesis (Patient II), exhibit modifications in blood flow behavior that require a specialized study.

In the simulation analysis, particularly in the proximal (CS1) and distal (CS2) sections of the aorta, it is evident that Patient I exhibits higher velocity values compared to Patient II, with significant variability during the systole phase. The increased variability in the distal segment of Patient II can be attributed to the irregular geometry of the aorta and the specific measurement locations. This variability suggests a lack of uniformity in the flow. While it's not possible to definitively conclude that this occurs at the junction of the prosthesis with the endothelium, these flow alterations can lead to an imbalance in the forces acting on the prosthesis, resulting in minor pressure fluctuations. When multiplied by the heart rate, such pressure variations can influence anatomical changes and potentially lead to prosthesis migration or disruption of prosthesis-endothelium continuity.

In both patients, a noticeable geometric alteration is observed in the aortic canal after the bifurcation (CS2). This alteration is significantly more pronounced in Patient II due to the presence of an aneurysm and its repair with an endovascular prosthesis. The distinct geometry in CS2 of Patient II results in a pressure differential of up to 10% of the nominal value (120 $mmHg$) due to the presence of vortices with varying speeds within the section, contributing to variations in shearing forces.

These variations in pressure and flow, when compounded by the heart rate, have the potential to generate a pressure differential that could be transmitted to the ends of the endoprosthesis. These forces may, in turn, induce anatomical deformations that hinder the secure anchorage of the prosthesis, thereby increasing the risk of unintended displacement or detachment.

It is important to note that these findings cannot be generalized without further study involving a larger patient population. Nevertheless, this proof of concept highlights a potential risk of endoprosthesis failure, which poses new challenges for the authors and sponsors of this study.

The results of simulations identifying low shear stresses detected in the proximal area of the endovascular prosthesis contribute to an increase in neointimal proliferation and, therefore, act as a favoring factor for restenosis.

The use of Computational Fluid Dynamics (CFD) techniques has allowed investigating, through simulations, the impact of complex anatomical geometries, such as those in TEVAR, on the hemodynamic behavior inside the aorta, becoming a tool for personalized clinical anomaly prevention and detection. The knowledge and quantification of variables such as velocity, pressure, and WSS in

specific zones of the aortic conduit provide valuable information for the development of preventive and corrective strategies for the patient existing pathologies.

The proposed mechanism for synchronizing the CT image acquisition process is suggested as an alternative solution to minimize artifacts resulting from the inherent movement of the heart. This allows for obtaining images suitable for evaluation with a 3D model of the aorta. Such images are valuable and reliable for characterizing the blood flow behavior of a specific patient.

CRediT authorship contribution statement

Juan P. Tello: Writing – review & editing, Writing – original draft, Visualization, Validation, Software, Investigation, Formal analysis, Conceptualization. **Juan C. Velez:** Writing – review & editing, Validation, Supervision, Methodology, Formal analysis, Conceptualization. **Alberto Cadena:** Writing – original draft, Validation, Methodology, Investigation, Funding acquisition, Conceptualization. **Andres Jutinico:** Writing – review & editing, Methodology. **Mauricio Pardo:** Writing – review & editing, Supervision, Methodology, Formal analysis. **Winston Percybrooks:** Writing – review & editing.

Declaration of competing interest

The authors declare that they have no known competing financial interests or personal relationships that could have appeared to influence the work reported in this paper.

Data availability

Data availability in https://uninorte-my.sharepoint.com/:f:/g/personal/telloj_uninorte_edu_co/EmuXWKeFsnNAuWY5CYfCwu4BRGOcbQi_MadMJxg7Czauqw?e=z4oVxr.

References

[1] W.H. Organization, Cardiovascular diseases (CVDs), https://www.who.int/news-room/fact-sheets/detail/cardiovascular-diseases-(cvds), 2021.
[2] A.H. Association, Actualización de estadísticas sobreenfermedades cardíacas y ataques o derrames cerebrales, año 2022, https://professional.heart.org/-/media/PHD-Files-2/Science-News/2/2022-Heart-and-Stroke-Stat-Update/Translated-Materials/2022-Stat-Update-at-a-Glance-Spanish.pdf, 2022.
[3] O.P.D.L. Salud, Las enfermedades del corazón siguen siendo la principal causa de muerte en las Américas, https://www.paho.org/es/noticias/29-9-2021-enfermedades-corazon-siguen-siendo-principal-causa-muerte-americas, 2021.
[4] B. Zhou, R.M. Carrillo-Larco, G. Danaei, L.M. Riley, C.J. Paciorek, G.A. Stevens, E.W. Gregg, J.E. Bennett, B. Solomon, R.K. Singleton, et al., Worldwide trends in hypertension prevalence and progress in treatment and control from 1990 to 2019: a pooled analysis of 1201 population-representative studies with 104 million participants, Lancet 398 (10304) (2021) 957–980.
[5] J.F. Figueroa Triana, D.A. Salas Márquez, J.S. Cabrera Silva, C.C. Alvarado Castro, A.F. Buitrago Sandoval, Covid-19 y enfermedad cardiovascular, Rev. Colomb. Cardiol. 27 (3) (2020) 166–174.
[6] S. Mendis, P. Puska, B.e. Norrving, W.H. Organization, et al., The underlying pathology of heart attacks and strokes, in: Global Atlas on Cardiovascular Disease Prevention and Control, World Health Organization, 2011, p. 14.
[7] S. Mendis, P. Puska, B.e. Norrving, W.H. Organization, et al., What are cardiovascular diseases (CVDs)?, in: Global Atlas on Cardiovascular Disease Prevention and Control, World Health Organization, 2011, p. 3.
[8] D.A. Steinman, Image-based computational fluid dynamics modeling in realistic arterial geometries, Ann. Biomed. Eng. 30 (4) (2002) 483–497.
[9] B. Šeta, M. Torlak, A. Vila, Numerical simulation of blood flow through the aortic arch, in: CMBEBIH 2017, Springer, 2017, pp. 259–268.
[10] C.A. Taylor, M.T. Draney, J.P. Ku, D. Parker, B.N. Steele, K. Wang, C.K. Zarins, Predictive medicine: computational techniques in therapeutic decision-making, Comput. Aided Surg. 4 (5) (1999) 231–247.
[11] N. Shahcheraghi, H. Dwyer, A. Cheer, A. Barakat, T. Rutaganira, Unsteady and three-dimensional simulation of blood flow in the human aortic arch, J. Biomech. Eng. 124 (4) (2002) 378–387.
[12] S. Lam, G.S. Fung, S.W. Cheng, K. Chow, A computational study on the biomechanical factors related to stent-graft models in the thoracic aorta, Med. Biol. Eng. Comput. 46 (11) (2008) 1129–1138.
[13] K.M. Tse, P. Chiu, H.P. Lee, P. Ho, Investigation of hemodynamics in the development of dissecting aneurysm within patient-specific dissecting aneurismal aortas using computational fluid dynamics (CFD) simulations, J. Biomech. 44 (5) (2011) 827–836.
[14] C.A. Taylor, D.A. Steinman, Image-based modeling of blood flow and vessel wall dynamics: applications, methods and future directions, Ann. Biomed. Eng. 38 (3) (2010) 1188–1203.
[15] D.J. Withey, Z.J. Koles, Medical image segmentation: methods and software, in: 2007 Joint Meeting of the 6th International Symposium on Noninvasive Functional Source Imaging of the Brain and Heart and the International Conference on Functional Biomedical Imaging, IEEE, 2007, pp. 140–143.
[16] N. Villain, Y. Goussard, J. Idier, M. Allain, Three-dimensional edge-preserving image enhancement for computed tomography, IEEE Trans. Med. Imaging 22 (10) (2003) 1275–1287.
[17] F.J. Calvo Plaza, Simulación del flujo sanguíneo y su interacción con la pared arterial mediante modelos de elementos finitos, Ph.D. thesis, Caminos, 2006.
[18] G. Vilalta, F. Nieto, M. Rodríguez, L. Laurentiu, J. OConnor, O. Dounié, Influence of abdominal aortic aneurysms geometry in the blood flow dynamics and in its rupture risk, Ing. Mec. 2 (2009) 29–37.
[19] H.-M. Hsiao, K.-H. Lee, Y.-C. Liao, Y.-C. Cheng, Hemodynamic simulation of intra-stent blood flow, Proc. Eng. 36 (2012) 128–136.
[20] M.L. Shrestha, A hemodynamic modelling of the blood circulation, Ph.D. thesis, 2016.
[21] A. Polańczyk, M. Strzelecki, T. Woźniak, W. Szubert, L. Stefańczyk, 3d blood vessels reconstruction based on segmented ct data for further simulations of hemodynamic in human artery branches, Found. Comput. Decision Sci. 42 (4) (2017) 359–371.
[22] S. Pasta, O. Dur, K. Pekkan, D.A. Vorp, J.S. Cho, Computer modeling for the prediction of thoracic aortic stent graft collapse, J. Vasc. Surg. 54 (3) (2011) 925.
[23] F. Auricchio, M. Conti, A. Lefieux, S. Morganti, A. Reali, F. Sardanelli, F. Secchi, S. Trimarchi, A. Veneziani, Patient-specific analysis of post-operative aortic hemodynamics: a focus on thoracic endovascular repair (TEVAR), Comput. Mech. 54 (2014) 943–953.
[24] M. Podyma, I. Zbicinski, Estimation of the effect of system geometry on blood flow hemodynamics in arteries, Inż. Chem. Proces. 25 (3) (2004) 1527–1532.
[25] L. Morris, P. Delassus, A. Callanan, M. Walsh, F. Wallis, P. Grace, T. McGloughlin, 3-d numerical simulation of blood flow through models of the human aorta, J. Biomech. Eng. 127 (5) (2005) 767–775.

[26] A. Tang, Y. Fan, S. Cheng, K. Chow, Biomechanical factors influencing type b thoracic aortic dissection: computational fluid dynamics study, Eng. Appl. Comput. Fluid Mech. 6 (4) (2012) 622–632.
[27] M. Dabagh, P. Vasava, P. Jalali, Effects of severity and location of stenosis on the hemodynamics in human aorta and its branches, Med. Biol. Eng. Comput. 53 (5) (2015) 463–476.
[28] F.P. Salvucci, C.A. Perazzo, S. Salles, J.G. Barra, R.L. Armentano, Influence of intel conditions in wall shear stress distributions of left coronary arteries in patient-specific simulations, Mec. Comput. 29 (59) (2010) 5953–5960.
[29] Q. Sun, J. Yang, S. Zhao, C. Chen, Y. Hou, Y. Yuan, S. Ma, Y. Huang, Live-net: comprehensive 3D vessel extraction framework in CT angiography, Comput. Biol. Med. (2023) 106886.
[30] W. Bracamonte-Baran, J. Bracamonte-Baran, M. Baritto-Loreto, A. D'Alessandro-Martínez, Dinámica de fluidos computacional aplicada al estudio del flujo sanguíneo en el cayado aórtico humano y sus principales ramas, Ing. Investig. Tecnol. 17 (1) (2016) 45–60.
[31] J.A. Moore, D.A. Steinman, C.R. Ethier, Computational blood flow modelling: errors associated with reconstructing finite element models from magnetic resonance images, J. Biomech. 31 (2) (1997) 179–184.
[32] J.A. Moore, Computational Blood Flow Modelling in Realistic Arterial Geometries, Graduate Department of Mechanical and Industrial Engineering, University of Toronto, 1998.
[33] J. Yin, Y. Xiang, Q. Dou, Three-dimensional reconstruction and numerical simulation of blood flow in human thoracic aortic, in: 2010 4th International Conference on Bioinformatics and Biomedical Engineering, IEEE, 2010, pp. 1–4.
[34] M.R. Labrosse, Cardiovascular Mechanics, CRC Press, 2018.
[35] G.S. Fung, S. Lam, S.W. Cheng, K. Chow, On stent-graft models in thoracic aortic endovascular repair: a computational investigation of the hemodynamic factors, Comput. Biol. Med. 38 (4) (2008) 484–489.
[36] J. Yang, Y. Hong, Numerical simulations of the non-Newtonian blood blow in human thoracic aortic dissection based on ct images, in: 2011 5th International Conference on Bioinformatics and Biomedical Engineering, IEEE, 2011, pp. 1–4.
[37] Y.-c. Fung, Biomechanics: Circulation, Springer Science & Business Media, 2013.
[38] T.J. Pedley, The Fluid Mechanics of Large Blood Vessels, Cambridge University Press, 1980.
[39] C.H. Armour, B. Guo, S. Pirola, S. Saitta, Y. Liu, Z. Dong, X.Y. Xu, The influence of inlet velocity profile on predicted flow in type b aortic dissection, Biomech. Model. Mechanobiol. 20 (2021) 481–490.
[40] M.S. Olufsen, C.S. Peskin, W.Y. Kim, E.M. Pedersen, A. Nadim, J. Larsen, Numerical simulation and experimental validation of blood flow in arteries with structured-tree outflow conditions, Ann. Biomed. Eng. 28 (11) (2000) 1281–1299.
[41] D. Obidowski, Blood flow simulation in human vertebral arteries, Ph.D. thesis, Technical University of Lodz, Lodz, 2007 (in Polish) (2007).
[42] R.-H. Kao, W.-L. Chen, C.-D. Kan, T.-S. Leu, Numerical simulation of blood flow crossing the aortic arch, in: 2013 1st International Conference on Orange Technologies (ICOT), IEEE, 2013, pp. 119–122.
[43] P. Reorowicz, D. Obidowski, P. Klosinski, W. Szubert, L. Stefanczyk, K. Jozwik, Numerical simulations of the blood flow in the patient-specific arterial cerebral circle region, J. Biomech. 47 (7) (2014) 1642–1651.
[44] Y. Zócalo, D. Bia, Presión aórtica central y parámetros clínicos derivados de la onda del pulso: evaluación no invasiva en la práctica clínica importancia clínica y análisis de las bases metodológicas de los equipos disponibles para su evaluación, Rev. Urug. Cardiol. 29 (2) (2014) 215–230.
[45] Z. Tyfa, D. Obidowski, P. Reorowicz, L. Stefańczyk, J. Fortuniak, K. Jóźwik, Numerical simulations of the pulsatile blood flow in the different types of arterial fenestrations: comparable analysis of multiple vascular geometries, Biocybern. Biomed. Eng. 38 (2) (2018) 228–242.
[46] M. Bechel, G. Noble, R. Ratliff, R. Hart, Fluid-structure interaction in a network of blood vessels, 2005.
[47] K. Jozwik, D. Obidowski, Numerical simulations of the blood flow through vertebral arteries, J. Biomech. 43 (2) (2010) 177–185.
[48] S. Miori, R. Repetto, M. Tubino, A one-dimensional model of bifurcations in gravel bed channels with erodible banks, Water Resour. Res. 42 (11) (2006).
[49] D. Katritsis, L. Kaiktsis, A. Chaniotis, J. Pantos, E.P. Efstathopoulos, V. Marmarelis, Wall shear stress: theoretical considerations and methods of measurement, Prog. Cardiovasc. Dis. 49 (5) (2007) 307–329.
[50] M. Zhou, Y. Yu, R. Chen, X. Liu, Y. Hu, Z. Ma, L. Gao, W. Jian, L. Wang, Wall shear stress and its role in atherosclerosis, Front. Cardiovasc. Med. 10 (2023) 1083547.
[51] R. Mongrain, J. Rodés-Cabau, Papel de la tensión de cizallamiento en la enfermedad aterosclerótica y la reestenosis tras implantación de stent coronario, Rev. Esp. Cardiol. 59 (1) (2006) 1–4.
[52] J. Rivera, F. Arias, A. Badrenas, J. Grau, Estudio hemodinámico mediante simulación numérica para completar el diagnóstico en estenosis carotídeas tributarias de endarterectomía, Rev. Int. Métodos Numér. Cálc. Diseño Ing. 32 (2) (2016) 125–130.
[53] P.A. Holme, U. Ørvim, M.J. Hamers, N.O. Solum, F.R. Brosstad, R.M. Barstad, K.S. Sakariassen, Shear-induced platelet activation and platelet microparticle formation at blood flow conditions as in arteries with a severe stenosis, Arterioscler. Thromb. Vasc. Biol. 17 (4) (1997) 646–653.
[54] C. Slager, J. Wentzel, F. Gijsen, J. Schuurbiers, A. Van der Wal, A. Van Der Steen, P. Serruys, The role of shear stress in the generation of rupture-prone vulnerable plaques, Nat. Clin. Pract. Cardiovasc. Med. 2 (8) (2005) 401–407.
[55] P.H. Stone, A.U. Coskun, S. Kinlay, M.E. Clark, M. Sonka, A. Wahle, O.J. Ilegbusi, Y. Yeghiazarians, J.J. Popma, J. Orav, et al., Effect of endothelial shear stress on the progression of coronary artery disease, vascular remodeling, and in-stent restenosis in humans: in vivo 6-month follow-up study, Circulation 108 (4) (2003) 438–444.